Additional information.

A. Benchmark Calculation.

The system presented in section 3.1 was calculated with similar initial concentrations (see table 1 for the reaction network and table 2 for the initial conditions) and temperature but in this case, concentration change of all chemical species were calculated, these settings translate into $^{d[x]}/_{dt} \neq 0$ and therefore calculated for all species. Figs A. 1 panels a and b show the time evolution of all chemical species involved in the simulation.

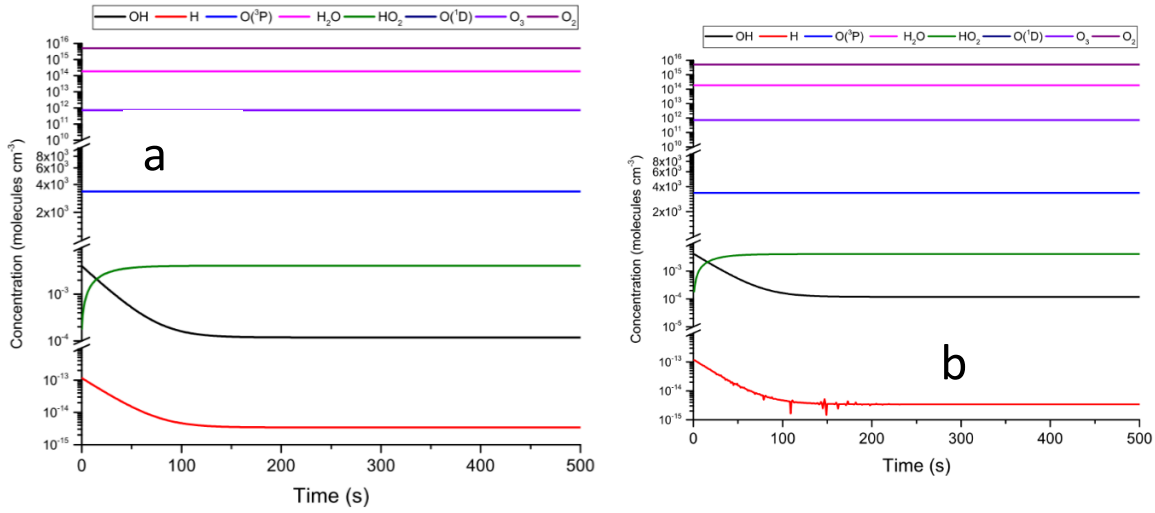

Figure A.1: Time evolution for the chemical network presented in table 1 as calculated with the KROME code (panel a) and the PATMO code (panel b). The reproducibility of this simple 0-dimensional system is to ensure that production-depletion equations are calculating properly calculating the chemical change of the considered chemical network.

B. Photo-dissociation of a single chemical species at different altitudes

In this section the ability of the code to calculate photo-dissociation rate constants was investigated and compared to KROME. For this study, the system was purposefully kept to a minimal number of reactions ($SO_2 \rightarrow SO + O$) so the calculation of photo-dissociation rate constants can be monitored, analyzed, and compare to a KROME simulation. For this study KROME was set to calculate 100 different boxes in which the opacity term (Eqn. 4) calculation of the of each layer, starting from the top, is the boundary condition of the layer beneath. Since this system does not take transport into consideration no further assumptions are required. The calculation of the photo-dissociation rate constant (Eqn. 2) is very sensitive to the opacity term. This sensitivity is the cause of the differences observed between Figs. 3 a and b. This analysis is conducted only for PATMO, but we verified that KROME produced similar results. Figure A. 2 shows photo-dissociation rate constants (right vertical axis) and

number density (left vertical axis) as time evolves. Panel a in Fig. A. 2 shows the results for the upper part of the atmosphere (91 km), while panel b shows the results for the bottom. The difference of these two plots shows that the photo-dissociation rate constants is not affected at the top of the atmosphere due to thin (low pressure) conditions. Conversely panel b shows that the photo-dissociation rate constant is very small, due to the shielding of the upper layers, and after most of the SO_2 column has been depleted (Fig. 3 panel a) the opacity term becomes zero and the photo-chemistry of this layer accelerates.

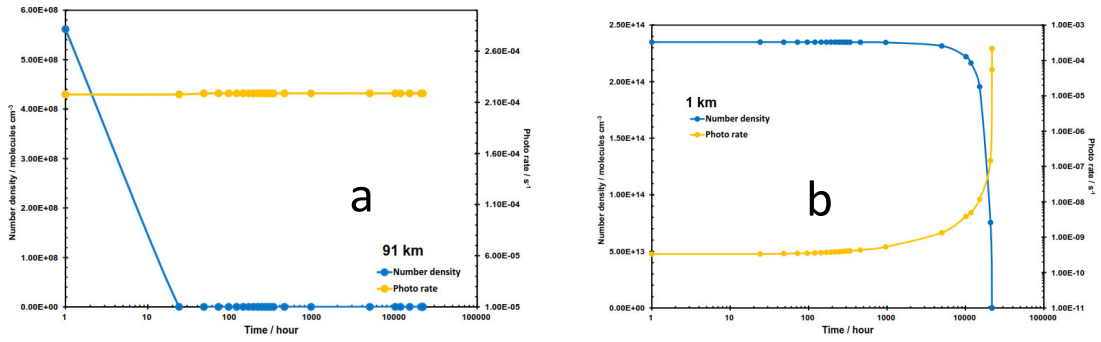

Figure A.2: Time evolution of SO_2 Number density (left vertical axis) and photo dissociation rate constant (vertical right axis) calculated at for 91 km (panel a) and 1 km (panel b).

C. Oxygen photo-dissociation and isotopic effects

The isotopic effect during its photo-dissociation reaction is produced by a complex interaction of spectral features. Figure A. 3 shows spectra of 3 isotopologues at 3 different spectral resolutions. A naked eye inspection of these spectra suffices to see how the degraded lower resolution spectra of panes a, b and c would create artifacts in the computation of photo-dissociation induced isotopic effects. Fig. A. 4 presents the spectra of panel d in Fig. S3 compared to the UV solar flux at the top of the atmosphere. From Eqn. 2 the total photo-dissociation rate constant is the integration over a designated energy range, where it can be observed that the isotopic effect is born out of complex interaction of light flux, cross-sections, and self-shielding. The Oxygen isotopes UV absorption cross-sections were estimated from spectral data reported by (Yoshino et al., 1987). Since the isotopic spectra used in this analysis is raw estimate the isotopic fractionation constants calculated here are not reliable for geochemical predictions.

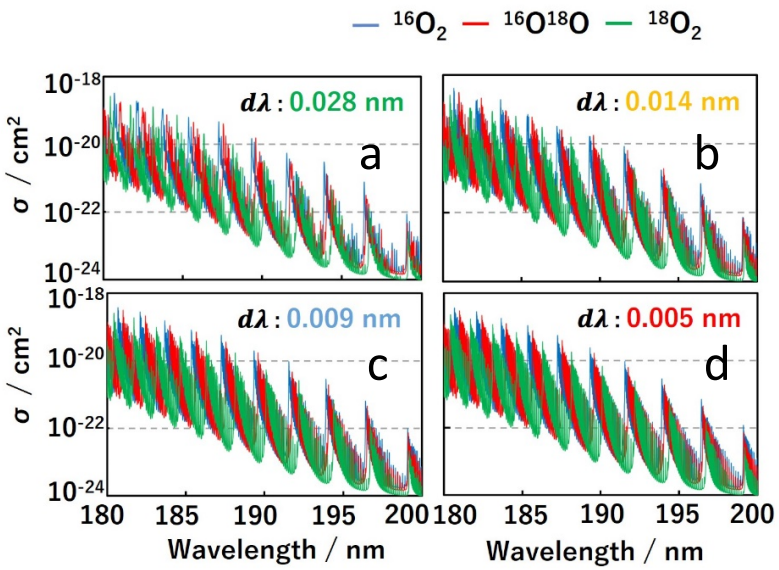

Figure A.3: UV absorption cross-sections for $^{16}O_2$, $^{16}O^{18}O$ and $^{18}O_2$ isotopologues at four different spectral resolutions 0.028 nm (panel a), 0.014 nm (panel b), 0.009 nm (panel c), 0.005 nm (panel d)

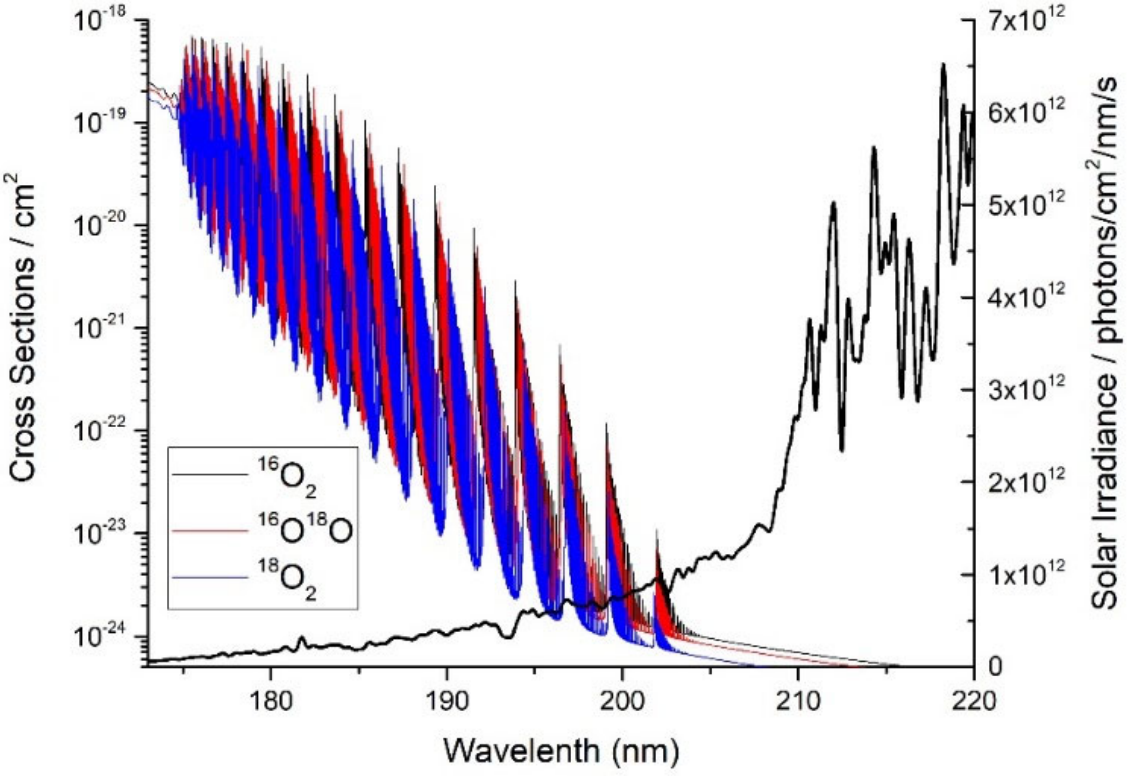

Figure A.4: UV absorption cross-sections for three different Oxygen isotopes ($^{16}O_2$, $^{16}O^{18}O$ and $^{18}O_2$) with a 0.005 nm spectral resolution (left vertical axis) and solar flux as reported by (Gueymard, 2004).

D. Reproducibility of today's Earth Atmosphere

The following information present details that were abbreviated in the main text. The atmospheric temperature (Krueger and Minzner, 1976) and Eddy diffusion coefficients (Massie and Hunten, 1981) are shown in fig. A.5. Species that were provided with a fixed concentration throughout the simulation (Goody and Yung, 1995 and Sen et al., 1998) are show in fig. A.6. Fig. A.7 shows calculated solar fluxes with an extended Chapman model (main text section 3.5) compared to data modeled by McLinden et. al., (2002), modeled profiles mostly replicate the literature profile except for the 180-200 nm range. The observed differences can be attributed to differences in UV absorption spectral data of O_2 in the Schuman-Runge bands. Fig. A.8 shows a time evolution of the modeled solar since the beginning of the simulation (t_0) where O_3 is not present in the atmosphere (Fig. A.8a), the shielding the of the solar flux is due to O_2 Schuman-Runge band and Herzberg continuum. Panels b and c show how the increased levels of O_3 at 1 day and 10 years of simulation time where increased concentrations of O_3 and NO_x compounds produce fluxes with similar features to the current atmosphere. Fig. A.9 shows the time evolution of photo-dissociation rates for all photoactive species (O_3, O_2, NO_2, N_2O, HNO_3, H_2O, NO_3 and N_2O_5)

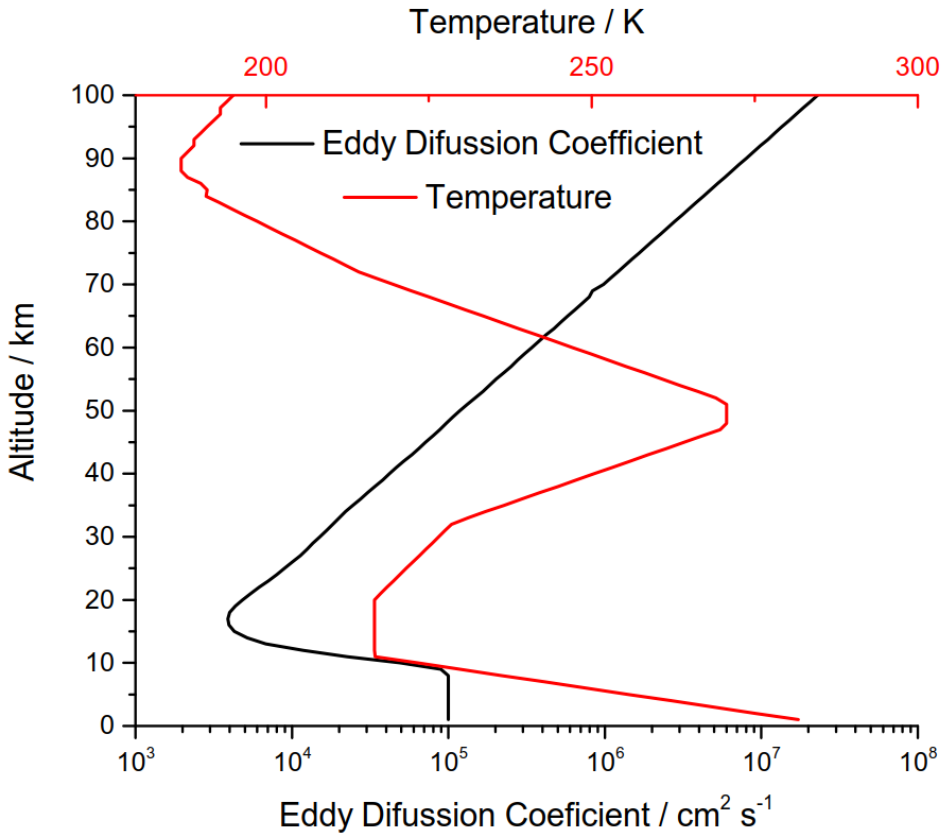

Figure A.5: Altitude profile for the Eddy diffusion coefficients shown in black solid line with bottom vertical axis (Massie and Hunten (1981) and temperature profile shown in solid red line and top vertical axis (*U.S. Standard Atmosphere, 1976*, Krueger and Minzner, 1976) used in both KROME and PATMO codes. Eddy diffusion coefficient are derived from the number density profile of trace gases (Massie and Hunten 1981).

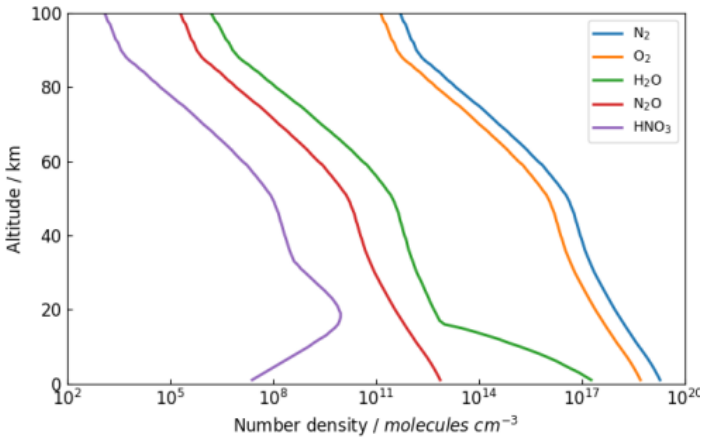

Figure A.6: Boundary conditions for the simple and extended Chapman mechanism presented in section 3.5. Chemical species with fixed concentrations throughout the simulation. N_2 and O_2 were set to 21% and 78% of the total mixing ratio, N_2O, H_2O, and HNO_3 profiles were taken from Goody and Yung, (1995) and Sen et al., (1998) respectively.

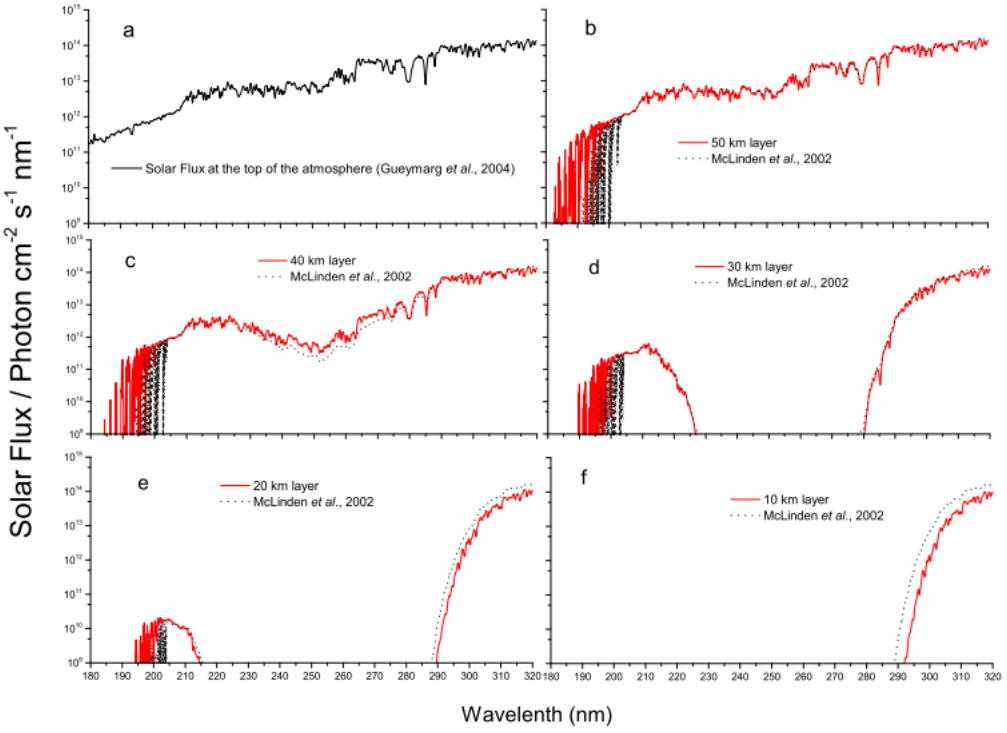

Figure A.7: Solar flux modeled with an extended Chapman model and compared to literature data. The data in panel a is the boundary conditions for our simulation and that is the solar flux at the top of the atmosphere (Gueymard, 2004). Panels b to f show modeled solar flux at 50, 40, 30, 20, and 10 km respectively and compared to literature data by (McLinden et al., 2002).

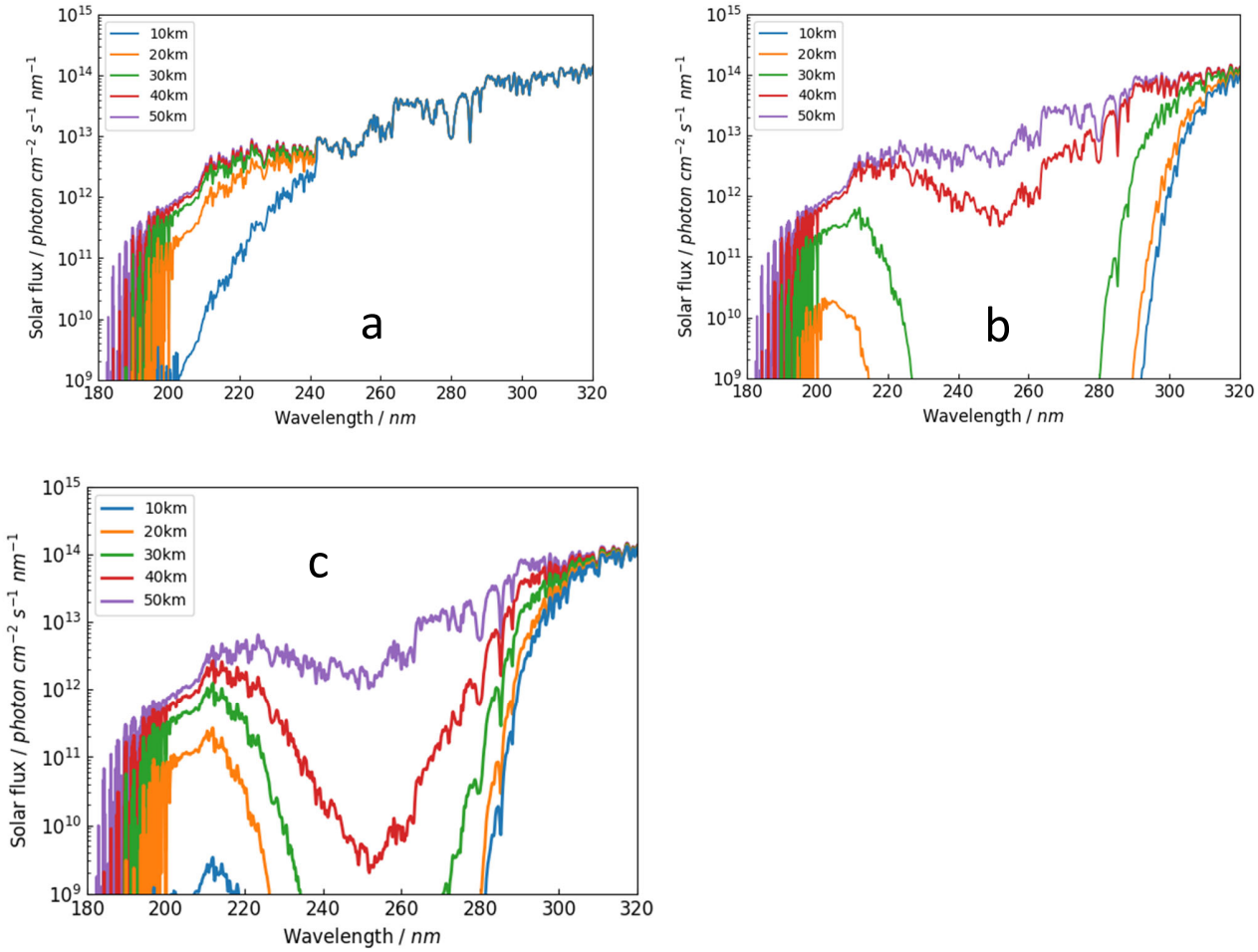

Figure A.8: Panels a to c show the evolution of the solar actinic flux as a function of time for the simple Chapman mechanism presented in section 3.5. The initial conditions for this simulation consider an atmosphere with 21% of O_2 as the only UV light absorber. Panel a shows the solar flux affected by Oxygen, as set by the initial settings and the incidence of O_3 as its mixing ratios are increased with the evolution of chemical species. Panels a, b and c represent fluxes at time 0, 1 day and 10 years respectively.

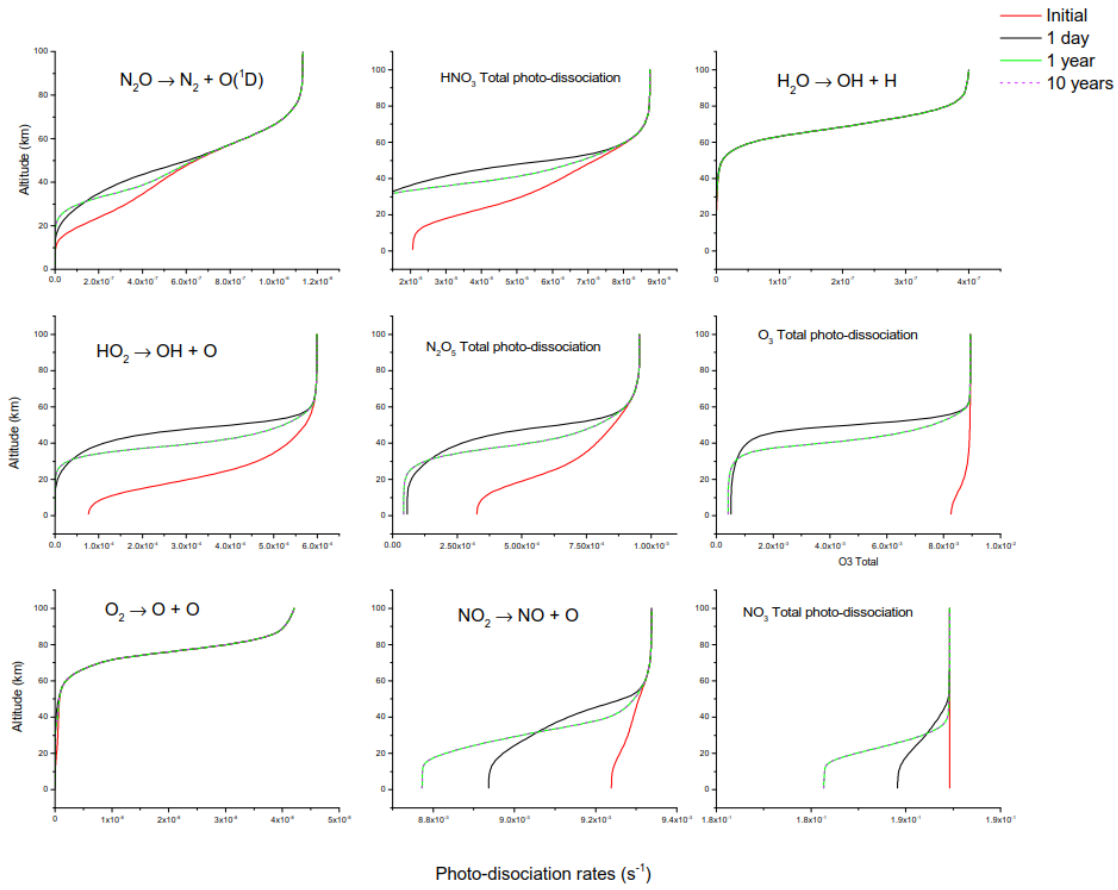

Figure A.9: Photo-dissociation rate constants profile and their time evolution of all photo-active species considered in the extended Chapman model. All panels in the figure show initial conditions (t_0, red line), 1 day (black line), 1 year (green line) and 10 years (dotted purple line) of simulated time. After 1 year of simulated time, the rate constant profile does not change significantly indicating the stability of the steady state condition.

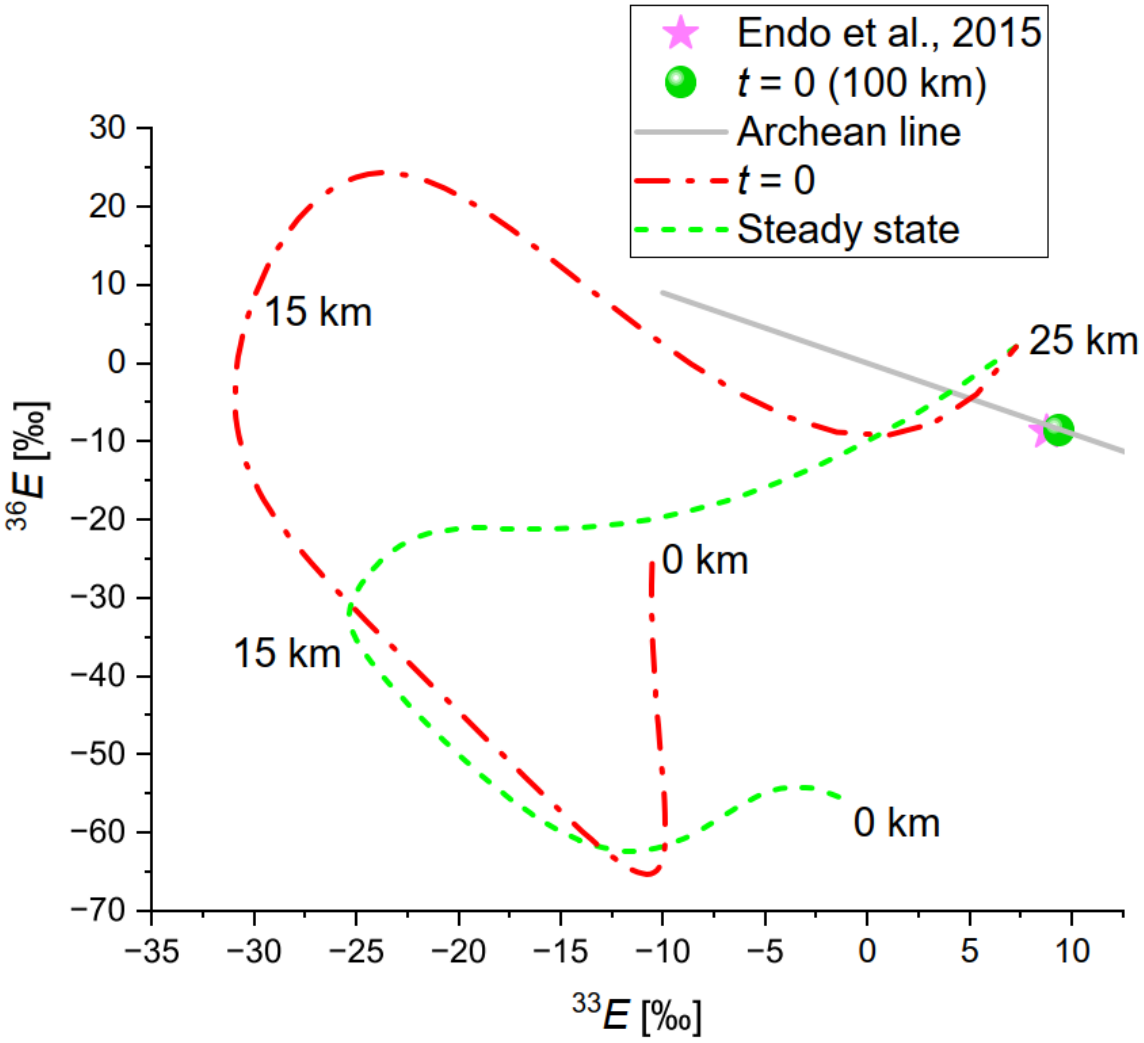

Fig. A. 10: Variation of the $^{33}E/^{36}E$ relation al function of altitude for initial and steady state conditions for a SO_2/SO photodissociation system as presented in section 3.4. For reference the Archean line as presented in Endo et al., (2015), $^{33}E/^{36}E$ values under pure shielding-less photodissociation (Endo et al., 2015) and at the top of the atmosphere (100 km).

References:

Brasseur, G. P. and Solomon, S. (2005) *Aeronomy of the Middle Atmosphere.* Springer Dordrecht.

Endo, Y., Danielache, S. O., Ueno, Y., Hattori, S., Johnson, M. S., Yoshida, N., Kjaergaard, H. G. (2015) Photoabsorption Cross-Section Measurements of ^{32}S, ^{33}S, ^{34}S, and ^{36}S Sulfur Dioxide from 190 to 220 nm. *J. Geophys. Res. Atmospheres* 120, 2546–2557. https://doi.org/10.1002/2014JD021671

Goody, R. M. and Yung, Y. L. (1995) Atmospheric Radiation: Theoretical Basis, Oxford University Press, New York.

Gueymard, C. A. (2004) The Sun's Total and Spectral Irradiance for Solar Energy Applications and Solar Radiation Models. *Sol. Energy* 76, 423–453. https://doi.org/10.1016/j.solener.2003.08.039

Krueger, A. J. and Minzner, R. A. A (1976) Mid-Latitude Ozone Model for the 1976 U.S. Standard Atmosphere. *J. Geophys. Res*. 81, 4477–4481. https://doi.org/10.1029/JC081i024p04477

Massie, S. T. and Hunten, D. M. (1981) Stratospheric Eddy Diffusion Coefficients from Tracer Data. *J. Geophys. Res. Oceans*, 86, 9859–9868. https://doi.org/10.1029/JC086iC10p09859

McLinden, C. A., McConnell, J. C., Griffioen, E. and McElroy, C. T. A (2002) A vector Radiative-Transfer Model for the Odin/OSIRIS Project. *Can. J. Phys.* 80, 375–393. https://doi.org/10.1139/p01-156

Sen, B., Toon, G. C., Osterman, G. B., Blavier, J.-F., Margitan, J. J., Salawitch, R. J. and Yue, G. K. (1998) Measurements of Reactive Nitrogen in the Stratosphere. *J. Geophys. Res. Atmospheres* 103, 3571–3585. https://doi.org/10.1029/97JD02468

Yoshino, K., Freemen, D. E., Esmond, J. R. and Parkinson, W. H. (1987) High Resolution Absorption Cross-Sections and Band Oscillator Strengths of the Schumann-Runge Bands of Oxygen at 79 K. *Planet. Space Sci*. 35, 1067–1075. https://doi.org/10.1016/0032-0633(87)90011-0